Materials Chemistry and Physics 208 (2018) 112–122

Contents lists available at ScienceDirect

Materials Chemistry and Physics

journal homepage: www.elsevier.com/locate/matchemphys

Novel NRGO-$CoWO_4$-Fe_2O_3 nanocomposite as an efficient catalyst for dye degradation and reduction of 4-nitrophenol

Mohamed Jaffer Sadiq Mohamed [a], Sandhya Shenoy U [b], D. Krishna Bhat [a, *]

[a] Department of Chemistry, National Institute of Technology Karnataka Surathkal, Mangalore 575025, India
[b] Department of Chemistry, College of Engineering and Technology, Srinivas University, Mukka, Mangalore 574146, India

HIGHLIGHTS

- A simple microwave synthesis of NRGO-$CoWO_4$-Fe_2O_3 nanocomposites for photocatalysis.
- High photocatalytic activity towards degradation of MB dye.
- Reduction of 4-NP to 4-AP in 30 seconds.
- Excellent stability and recyclability.

GRAPHICAL ABSTRACT

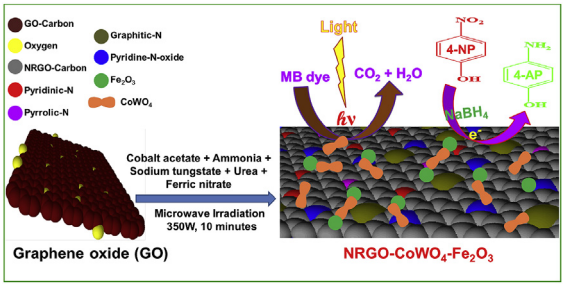

ARTICLE INFO

Article history:
Received 19 April 2017
Received in revised form
24 December 2017
Accepted 6 January 2018
Available online 9 January 2018

Keywords:
NRGO
Methylene blue
Reduction
Dye degradation
Organic pollutants

ABSTRACT

Novel NRGO-$CoWO_4$-Fe_2O_3 (N-doped reduced graphene oxide-cobalt tungstate-iron oxide) ternary nanocomposite was prepared by using simple microwave method. The synthesized materials were thoroughly characterized by X-ray diffraction (XRD) studies, Brunauer-Emmett-Teller (BET) analysis, transmission electron microscopy (TEM), high-resolution transmission electron microscopy (HRTEM), X-ray photoelectron spectroscopy (XPS), Raman spectroscopy, photoluminescence (PL) and UV-Visible spectroscopy. The nanocomposite was studied for its catalytic activity in degradation of methylene blue (MB) and reduction of 4-Nitrophenol (4-NP) to 4-Aminophenol (4-AP). The observed results of catalytic efficiency and rate constants indicated that the NRGO-$CoWO_4$-Fe_2O_3 nanocomposite can perform as an excellent catalyst compared to other composite materials. The detailed experimental study revealed that this ternary nanocomposite shows a great promise as a candidate for various environmental applications.

1. Introduction

Semiconductors and their nanocomposites are used in a variety of applications such as sensors, drug delivery, energy storage and as catalysts for several commercially significant reactions due to their catalytic nature [1]. If a composite material is useful in more than one industrial or commercial applications, then such a material would be of great interest and importance to the scientific community. They can also have an enormous influence on the economy and the environment. Until now, the practical applications of many catalysts are restricted due to some inherent difficulties such as the fast recombination rate of photo-generated electron-hole pairs, limited visible light responses, poor adsorptive performance, low efficiency, non-reusability and high cost [2,3]. In order to overcome

* Corresponding author.
E-mail address: kishan@nitk.edu.in (D.K. Bhat).

https://doi.org/10.1016/j.matchemphys.2018.01.012
0254-0584/

these drawbacks, it is necessary to develop nanocomposite materials using simple techniques which can be used for environmental applications.

In recent years, a combination of semiconductors with different phases have attracted great attention in catalytic research involving mixtures of metals, oxides, sulfides and tungstates [2–10]. These materials have better charge separation carriers and a fast electron transfer system compared to the pristine semiconductor materials. However, excellent catalytic performance with high stability and low cost are still rare. In order to achieve excellent catalytic performance in semiconductor nanocomposites with the above properties, we need to consider two key factors: faster electron transfer and better charge separation [11,12]. Reduced graphene oxide (RGO) is incorporated into semiconductors to assist the electron transfer and charge separation. A combination of semiconductors with suitable band gaps is also used to promote charge carrier separation and to obtain excellent catalytic performance.

$CoWO_4$ is considered as one of the most important class of metal tungstates with Wolframite structure, which has been used in the field of luminescence, energy conversion, energy storage, optical fibers, ceramics and photocatalysis [10,13–15]. There are many methods for the preparation of $CoWO_4$ such as Czochralski, hydrothermal, sol-gel, solid state and chemical precipitation methods [13–15]. However, the practical application of $CoWO_4$ is hindered due to high recombination rate and charge transfer.

RGO on the other hand is a 2D material formed by sp^2-bonded carbon atoms tightly packed into a two-dimensional hexagonal lattice and it is known for its large surface area, chemical strength, mechanical, optical, electrical and thermal properties [16–18]. It has extensive applications in fields such as catalysis, composites, biomaterials, nanoelectronic devices, Li-ion batteries, sensors and drug delivery [19–22]. The incorporation of electron-rich nitrogen atoms into the reduced graphene oxide materials promotes the interaction between neighboring carbons and electrons, providing a superior heteroatom-doped catalyst [8,9,23]. Nitrogen doped reduced graphene oxide (NRGO) increases the transfer rate of electron from the conduction band of the semiconductor whereas, the doping of nitrogen into semiconductors creates an additional donor level above the valence band of semiconductors thereby reducing the energy requirement for the excitation of electron from valance band (VB) to conduction band (CB) of semiconductor materials. The semiconductor materials supported on NRGO show significant enhancement in their catalytic performance [8,9,23].

Semiconductor materials like ZnO, NiO, Fe_2O_3, Fe_3O_4 are used in catalytic studies for their excellent stability and large surface area for absorption capability [3]. Recently, Fe_2O_3 based semiconductor nanoparticles were found to have excellent catalytic property due to their unique recombination rates and charge carrier separation which led to the improvement in catalytic efficiency [10,24]. Therefore, we thought Fe_2O_3 could be a good candidate for coupling with $CoWO_4$ and NRGO to form NRGO-$CoWO_4$-Fe_2O_3 composite with high catalytic activity. Also, to the best of our knowledge, there are no reports available on synthesis of NRGO-$CoWO_4$-Fe_2O_3 ternary nanocomposites using microwave irradiation method and their catalytic studies.

In continuation of our research work [8–10,24] in the field of nanocomposites using greener, fast synthetic method and various environmental catalytic applications, we report for the very first time, the synthesis of NRGO-$CoWO_4$-Fe_2O_3 ternary nanocomposites by microwave irradiation method. The synthesized materials were characterized by XRD, BET, TEM, HRTEM, XPS, Raman, PL and UV-Visible spectroscopy. The catalytic activity of the ternary nanocomposites was tested for photodegradation of MB under the visible light source and also examined for reduction of 4-NP to 4-AP using sodium borohydride reactions. The study suggests that the resulting NRGO-$CoWO_4$-Fe_2O_3 ternary nanocomposite shows excellent catalytic activity compared to the other composite materials. This makes $CoWO_4$ based ternary nanocomposite a promising material for various environmental applications.

2. Experimental

The schematic representation of the synthesis of NRGO-$CoWO_4$-Fe_2O_3 ternary nanocomposites is shown in Scheme 1.

2.1. Materials and methods

All the chemicals were purchased from Sigma-Aldrich and used without further purification. All the reactions were carried out with Millipore water.

2.2. Synthesis of graphene oxide (GO)

GO was synthesized by using a modified Hummers method [9]. In brief, 5 g of natural graphite flasks and 2.5 g of $NaNO_3$ was added in 150 mL of concentrated sulfuric acid under constant stirring in a beaker immersed in an ice water bath. Then, 15 g of $KMnO_4$ was added slowly and the mixture was stirred at the 30 °C for 2 h. Later, 230 mL of distilled water was added, and the mixture was further stirred for 30 min at 95 °C. Finally, 420 mL of distilled water and 10 mL of H_2O_2 were subsequently added to terminate the reactions. The color of the solution turned from dark brown to yellow. The obtained GO was separated by centrifugation, and washed.

2.3. Synthesis of $CoWO_4$

0.05 M of cobalt acetate was dissolved in 50 mL of DI water. Then 50 mL of 0.05 M of sodium tungstate solution was slowly added to the above solution under constant stirring for about 2 h. The resulting mixture was treated with microwave irradiation at 350 W for 10 min and then allowed to cool to room temperature. The formed precipitate of $CoWO_4$ was collected and washed with 10% ethanol several times and finally dried.

2.4. Synthesis of Fe_2O_3

0.005 M of ferric nitrate was dissolved in 50 mL of DI water. Then, 0.4 g of urea was added under constant stirring. Later, the reaction mixture was treated with microwave irradiation at 350 W for 10 min. Fe_2O_3 precipitate formed was collected and washed several times with 10% ethanol and later dried.

2.5. Synthesis of $CoWO_4$-Fe_2O_3

In a typical synthesis, 0.05 M of cobalt acetate was dissolved in 50 mL of DI water. Then 50 mL of 0.05 M of sodium tungstate solution was slowly added to the above solution under constant stirring for about 2 h 0.005 M of ferric nitrate was dissolved in 50 mL of DI water and then added to the above solution mixture. Then, 0.4 g of urea was added under constant stirring. The reaction mixture was treated with microwave irradiation at 350 W for 10 min. The precipitate of $CoWO_4$-Fe_2O_3 was washed with 10% ethanol and dried.

2.6. Synthesis of NRGO

NRGO was synthesized by a one-step microwave irradiation method. Urea was used as doping agent for nitrogen. In a typical synthesis, a calculated amount of GO was dispersed in the ethylene glycol solution (50 mL) under ultrasonic treatment for about 30 min

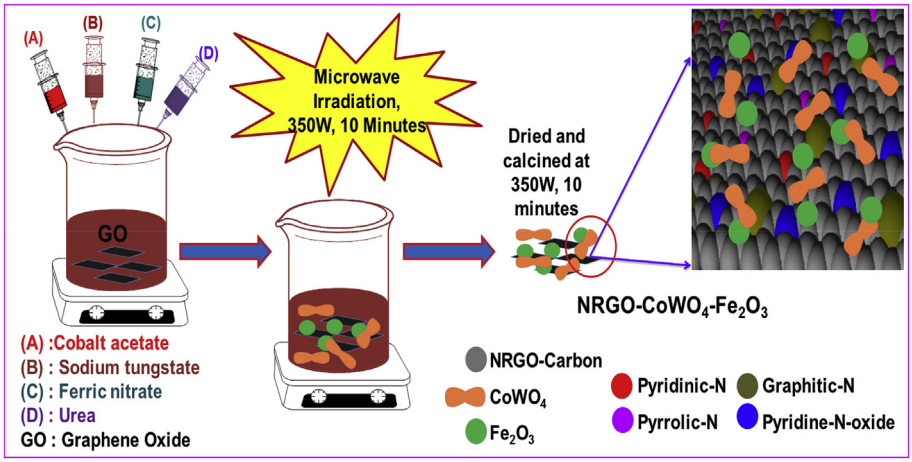

Scheme 1. Schematic representation of synthesis of NRGO-$CoWO_4$-Fe_2O_3 ternary nanocomposites.

1.0 g of urea was then added under constant stirring. The pH of the solution was maintained at 9.0 using required amount of ammonia solution. After 2 h, the mixture was treated with microwave irradiation at 350 W for 10 min and then the mixture was allowed to cool to room temperature. The formed NRGO was washed several times with DI water and 10% ethanol and then finally dried.

2.7. Synthesis of NRGO-$CoWO_4$

A calculated amount of GO (0.5, 1, 2.5, 5 wt. %) was dispersed in the ethylene glycol solution under ultrasonic treatment for about 30 min and 50 mL of 0.05 M of cobalt acetate solution was added to the above solution. Then, 50 mL of 0.05 M of sodium tungstate solution was slowly added to the reaction mixture and 1.0 g of urea was added under constant stirring. The pH of the solution was maintained at 9.0 using ammonia. After 2 h, the mixture was treated with microwave irradiation at 350 W for 10 min and then the mixture was allowed to cool to room temperature. NRGO-$CoWO_4$ was washed several times with DI water and 10% ethanol and then finally dried.

2.8. Synthesis of NRGO-$CoWO_4$-Fe_2O_3

aNRGO-$CoWO_4$-Fe_2O_3b nanocomposites were synthesized by a one-step microwave irradiation method similar to the procedure reported earlier by our group (a = 0.5, 1, 2.5, 5 wt.% of GO and b = 0.005, 0.01, 0.02 M of ferric nitrate) [8,9]. A calculated amount of GO was dispersed in the ethylene glycol solution under ultrasonic treatment for about 30 min and 50 mL of 0.05 M of cobalt acetate solution was added to the above solution. Then 50 mL of 0.05 M of sodium tungstate solution was slowly added to the reaction mixture and 1.0 g of urea was added under constant stirring while maintaining the pH at 9.0 using ammonia. To this mixture, designated amount of ferric nitrate dissolved in 50 mL of DI water was added. Later, 0.4 g of urea was added under constant stirring. This was irradiated with microwave at 350 W for 10 min. The obtained product of NRGO-$CoWO_4$-Fe_2O_3 composite was washed with 10% ethanol and dried.

2.9. Characterization

The structural and elemental characterization of the as synthesized nanocomposites was performed using X-ray diffractometer (Rigaku, Japan), laser Raman microscope (Renishaw Invia) with a 532 nm excitation laser source and X-ray photoelectron spectroscopy (XPS, Multilab 2000 Thermo scientific, UK). The specific surface area was determined using Brunauer-Emmett-Teller (BET) method (SMART SORB 92/93, Smart Instruments Company Pvt. Ltd.). The surface morphology and optical properties were studied using transmission electron microscope (TEM, TecnaiG20), high-resolution transmission electron microscope (HRTEM, Tecnai), photoluminescence spectrometer (LS-55, Perkin Elmer Instruments) with a 280 nm excitation wavelength source and UV-Visible spectrophotometer (Analytik Jena). The total organic carbon concentration was measured using total organic carbon analyzer (TOC-V CSN, Shimadzu, Japan). Mass spectrometry data of the degraded samples were obtained using an LCMS-2020 (Shimadzu).

2.10. Determination of photocatalytic activity

The photocatalytic degradation of MB dye was performed using photoreactor under ambient atmospheric condition. The photoreactor was equipped with a 250 W Hg lamp fitted with a 400 nm cutoff filter, as a source for visible light irradiation. In these experiments, 200 mL of MB dye solution (10 mg/L) and photocatalyst (20 mg) was added to 500 mL of Pyrex glass beaker and stirred for about 30 min in dark to reach the adsorption-desorption equilibrium of the photocatalyst and MB. Then, the solution was exposed to the visible light irradiation. During photocatalytic studies, at regular time intervals 4 mL of the reacted MB solution was taken out and centrifuged. The obtained supernatant solution was used to measure the concentration of the MB solution through UV-Visible spectroscopic analysis at a wavelength of 664 nm. The percentage of degradation of dye was calculated as per equation (1).

$$\text{Percentage of degradation of dye} = [(Co - C)/Co] \times 100 \quad (1)$$

where, C_o is the initial absorbance and C is the absorbance at a given interval of time by the MB dye solution, respectively. Further, all the data presented are averages of three independent measurements.

2.11. Determination of total organic carbon (TOC)

The extent of mineralization of the dye was calculated using TOC analysis. The TOC content was analyzed before (TOC_o) and during the photocatalytic reaction at various time intervals (TOC_t). The percentage mineralization of the dye was calculated using equation (2).

Percentage Mineralization of the dye

$$= [(TOCo - TOCt)/TOCo] \times 100 \quad (2)$$

where, TOC_o is the initial concentration and TOC_t is the concentration of the dye solution at a given time interval, respectively. All the experiments were carried out following the same procedure for photocatalytic degradation mentioned above.

2.12. Trapping experiments

To determine the possible photocatalytic degradation mechanism, and to identify the most important species influencing the catalytic degradation, trapping experiments were carried out using various kinds of scavengers such as 1 mM of benzoquinone (BQ, a quencher of O_2^-), 10 mM of potassium iodide (KI, a quencher of h^+), 10 mM of silver nitrate ($AgNO_3$, a quencher of e^-) and 10 mM of ternary Butanol (TBA, a quencher of $OH^·$). All the investigations were carried out following the same procedure for photocatalytic degradation mentioned above.

2.13. Determination of catalytic reduction of 4-NP to 4-AP

The catalytic reduction activity of the as-prepared materials was tested by the reduction of 4-NP to 4-AP using $NaBH_4$ at ambient temperature. In brief, as-prepared catalysts (0.001 g) were introduced into 2.7 mL of 4-NP aqueous solution (0.1 mM) and 0.3 mL of $NaBH_4$ aqueous solution (0.1 M). After starting the reaction, every 10 s samples were collected, centrifuged to remove the residual materials and the supernatant liquid was analyzed at 400 nm using a UV-Vis spectrophotometer. The catalytic conversion percentage of 4-NP to 4-AP was calculated by using a relation similar to that of equation (1).

3. Results and discussion

3.1. Structural and elemental studies

Fig. 1 shows the XRD patterns of the as-synthesized GO, RGO, NRGO, $CoWO_4$, Fe_2O_3 and NRGO-$CoWO_4$-Fe_2O_3. The XRD pattern of graphite shows a sharp peak corresponding to the reflection from the (002) plane at $2\theta = 26.3^\circ$ with a d-spacing of 0.339 nm. Whereas, GO exhibits a slightly broader peak at 10.5° with a d-spacing of 0.842 nm matching with the reflection from the (002) plane. These patterns are very similar to those reported previously for graphite and GO [25]. The XRD pattern of RGO is quite different from graphite and GO, and shows a slightly broader peak at 22.6° which corresponds to the reflection from the (002) plane with a d-spacing of 0.365 nm, suggesting the reduction of GO [26]. Although the doping of nitrogen in NRGO is in a small amount, differences between RGO and NRGO can be clarified easily. In contrast to the XRD pattern of RGO, NRGO shows a relatively broader peak at 24.4° again corresponding to the reflection from the (002) plane with a d-spacing of 0.355 nm. The slight increase in the reflection angle for (002) plane in NRGO compared to that of RGO may be ascribed to the entry of nitrogen atoms into the crystal lattice of graphite causing the increased distance between the graphite layers [27].

$CoWO_4$ and Fe_2O_3 diffraction patterns well matched with JCPDS file numbers 15-0867 and 33-0664, respectively. Also, XRD traces of the NRGO-$CoWO_4$-Fe_2O_3 ternary nanocomposite had all peaks of $CoWO_4$ and Fe_2O_3 confirming their existence in the nanocomposite and hence confirming the formation of the ternary nanocomposite. However, carbon diffraction peak for NRGO could not be clearly identified in NRGO-$CoWO_4$-Fe_2O_3 ternary nanocomposite, which may be due to overlapping with peaks from other components apart from small quantity, weak intensity and exfoliated nature of NRGO in the composite [8,9].

Raman spectroscopy is widely employed to study the ordered/disordered crystal structures of carbon-based materials [8,9,28]. In Fig. 2, the Raman spectrum of GO reveals two important functions, the G mode at 1599 cm^{-1} springing up from the emission region of zone-center optical phonons and D mode at 1355 cm^{-1} arising from the doubly resonant disorder-precipitated mode. I_D/I_G is the ratio of intensities of the D and G bands and it is a measure of the relative concentration of neighborhood defects (particularly the sp^3 hybridized defects) as compared to the sp^2 hybridized GO domain ones. It can be noted that, before the microwave irradiation, the I_D/I_G ratio was 0.87 for GO. After the microwave irradiation treatment, the I_D/I_G ratio increases to 1.089, indicating more defect formation, which may be due to the reduction and conversion of GO to NRGO and exfoliation of graphitic domains. The I_D/I_G ratios of pure NRGO and NRGO-$CoWO_4$-Fe_2O_3 nanocomposite are 1.0899 and 0.9189, respectively. The incorporation of $CoWO_4$ and Fe_2O_3 on the defective sites of the NRGO, might have contributed to the reduction of defects and restoration of the basal plane conjugation on the

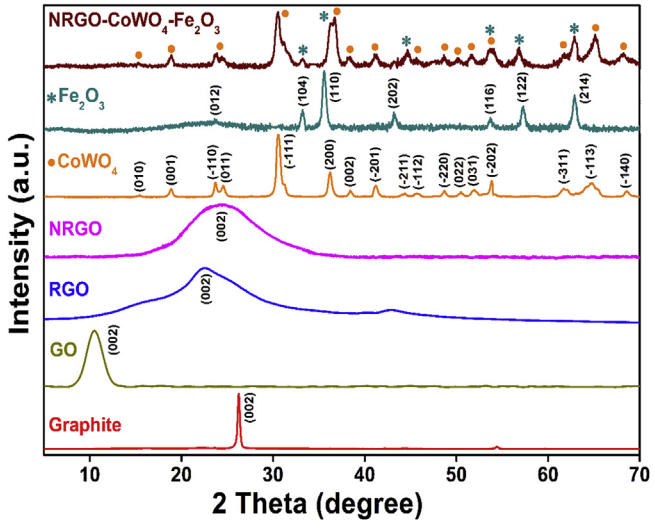

Fig. 1. XRD spectrum of GO, RGO, NRGO, $CoWO_4$, Fe_2O_3 and NRGO-$CoWO_4$-Fe_2O_3.

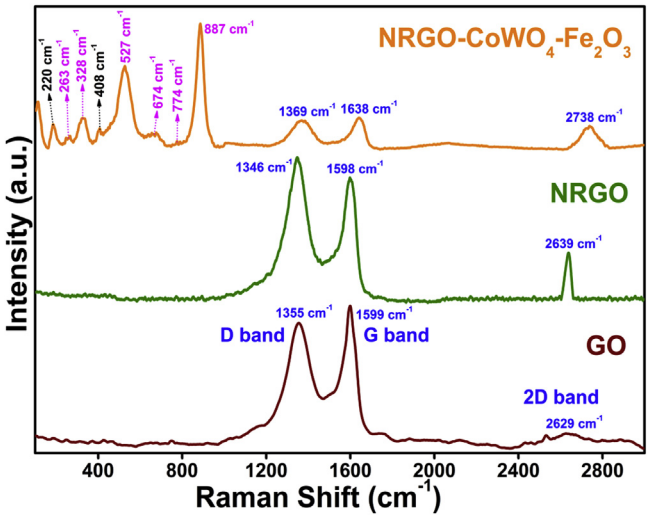

Fig. 2. Raman spectrum of GO, NRGO and NRGO-$CoWO_4$-Fe_2O_3.

surface of NRGO and this in turn might have caused a slight decrease in the I_D/I_G ratio of nanocomposite in comparison with the pure NRGO. Such observations are also available in literature [8,9].

The bands observed at 263 cm^{-1}, 328 cm^{-1}, 527 cm^{-1}, 674 cm^{-1}, 774 cm^{-1} and 887 cm^{-1} are ascribed to the six Raman active modes of $CoWO_4$, respectively [15]. Raman band at 220 cm^{-1} and 408 cm^{-1} are ascribed to the two Raman active modes of Fe_2O_3 [29]. Raman peaks of 1369 cm^{-1} (D band) to 1638 cm^{-1} (G band), with an I_D/I_G ratio 0.92 and the 2D band at 2738 cm^{-1} with I_{2D}/I_G ratio of 0.74, respectively are ascribed to NRGO.

The number of NRGO layers can be determined by the ratio I_{2D}/I_G, where I_{2D} is intensity of 2D band and I_G is intensity of G band. The ratio I_{2D}/I_G of >2, 1 to 2, and <1 corresponds to single, double and multi-layers of NRGO sheets, respectively [16]. In the present work I_{2D}/I_G is found to be 0.6634 and 0.7427 for NRGO and NRGO-$CoWO_4$-Fe_2O_3 nanocomposite, respectively. This suggests that the NRGO sheets are mostly of multilayered nature.

The chemical states of the essential elements of the NRGO-$CoWO_4$-Fe_2O_3 ternary nanocomposites were investigated via XPS analysis. The XPS survey spectrum and high-resolution spectrum of NRGO-$CoWO_4$-Fe_2O_3 ternary nanocomposites are as shown in Fig. S1 and Fig. 3, respectively. The binding energy states in the XPS spectrum have been calibrated with C *1s* region at 284.8 eV. The high-resolution C *1s* spectrum, is deconvoluted into six peaks at 284.54 eV (C=C), 286.04 eV (C-N), 286.93 eV (C-O-C), 288.58 eV (C=O), 289.97 eV (O-C=O) and 291.58 eV (π-π^* interaction), respectively [30]. The high-resolution N *1s* spectrum, is deconvoluted into four peaks at 398.77 eV (pyridinic-N), 400.14 eV (pyrrolic-N), 401.18 eV (graphitic-N) and 402.71 eV (pyridine-N-oxide), respectively [30]. The high-resolution Co *2p* spectrum, is deconvoluted into ten peaks located at 780.31 eV, 796.79 eV of Co^{3+} and 781.58 eV, 798.49 eV of Co^{2+}, which belongs to Co $2p_{3/2}$ and Co $2p_{1/2}$, respectively. And the satellite peaks of Co^{3+} are at 787.26 eV, 793.68 eV, 803.78 eV and that of Co^{2+} are at 784.10 eV, 790.37 eV, 801.99 eV, respectively [15]. The high-resolution W *4f* spectrum, which can be deconvoluted into four peaks at 34.92 eV and 37.03 eV, belongs to W $4f_{7/2}$ and W $4f_{5/2}$. And its satellite peaks are at 35.38 eV and 37.43 eV, respectively [15]. The high-resolution Fe *2p* spectrum are similarly deconvoluted into five peaks placed at 708.3 eV, 721.45 eV of Fe^{2+} and 710.67 eV, 724.18 eV of Fe^{3+} belongs to the Fe $2p_{3/2}$ and Fe $2p_{1/2}$. Its satellite peak is observed at 715.43 eV [9,10]. The high-resolution O *1s* spectrum is further deconvoluted into three peaks at 530.66 eV, 532.32 eV and 533.331 eV. These are related to Fe_2O_3, $CoWO_4$ and H-O-H bonds, respectively [8,9,15]. XPS also provides evidence for doping of N into RGO. Fig. S2 shows survey and high resolution XPS spectra for NRGO. The presence of N

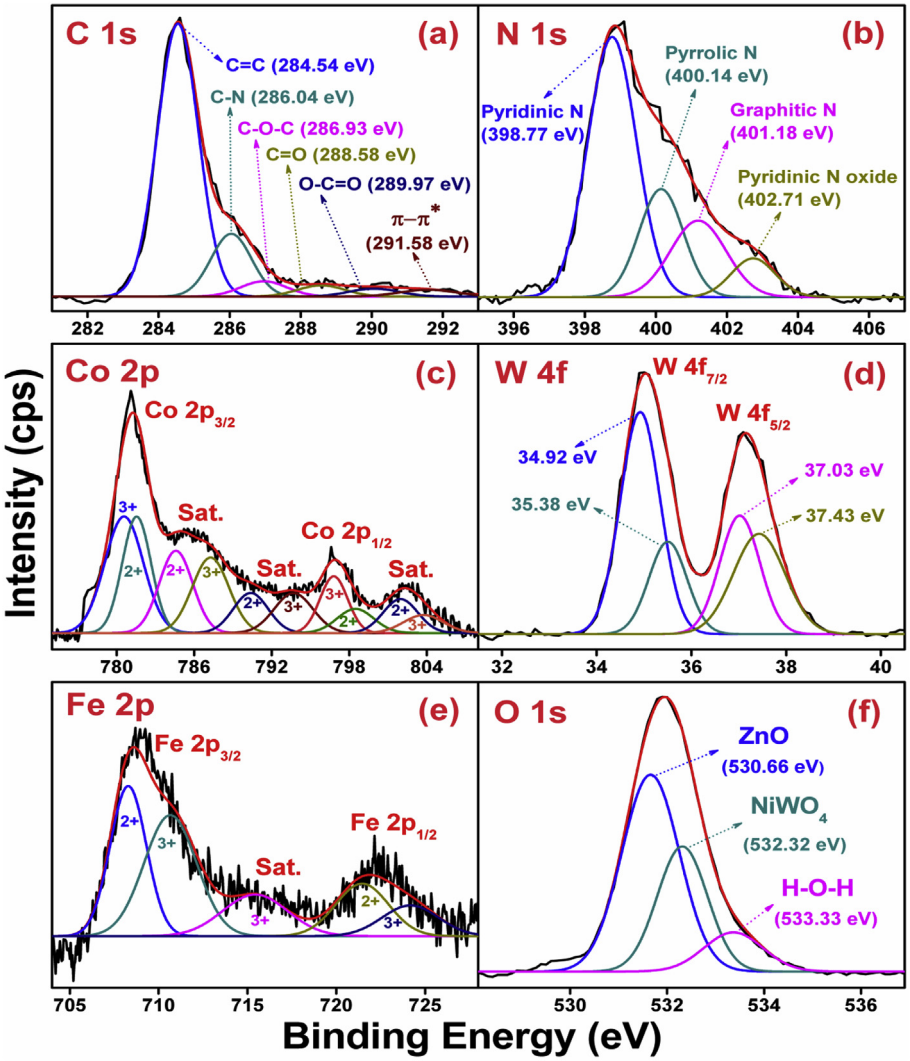

Fig. 3. XPS spectrum of NRGO-$CoWO_4$-Fe_2O_3 in the high-resolution region of C *1s*, N *1s*, Co *2p*, W *4f*, Fe *2p* and O *1s*.

could be clearly detected in the XPS spectra of NRGO, and the high-revolution N *1s* XPS spectra could be fitted into four types of N doping, such as, pyridinic N (398.3 eV), pyrrolic N (399.6 eV), graphite N (400.7 eV) and pyridinic N Oxide (402.5 eV) [8,9,11]. All the above results confirm the formation and presence of NRGO in the synthesized nanocomposite. The detailed composition values for C, N, Co, W, Fe and O in the ternary nanocomposite determined through XPS is given in Table S1.

3.2. Surface morphological and optical studies

The total surface area of $CoWO_4$, $CoWO_4$-Fe_2O_3 and NRGO-$CoWO_4$-Fe_2O_3 was determined from BET method. BET total surface area of $CoWO_4$, $CoWO_4$-Fe_2O_3 and NRGO-$CoWO_4$-Fe_2O_3 was 16.21 m^2g^{-1}, 22.25 m^2g^{-1} and 31.38 m^2g^{-1}, respectively. From these values, it is evident that introduction of NRGO nanosheets in the NRGO-$CoWO_4$-Fe_2O_3 nanocomposites increased the surface area compared to that of $CoWO_4$ and $CoWO_4$-Fe_2O_3. The increased surface area can contribute to the enhancement in the catalytic activity of the NRGO-$CoWO_4$-Fe_2O_3 nanocomposite along with reduction in their reaction time.

The structural morphology of the as-synthesized nanocomposites was analyzed by electron microscopy (Fig. 4). Fig. 4a shows the TEM image of the wrinkled sheet-like nature of N-doped RGO. Fig. 4b reveals small rod-like shapes of $CoWO_4$ with a wrinkled NRGO sheet. Fig. 4c shows NRGO-$CoWO_4$-Fe_2O_3 ternary nanocomposites containing 2D wrinkled sheet-like morphology of NRGO nanosheets, with approximately rod-like $CoWO_4$ and oval like Fe_2O_3 nanoparticles.

Fig. 4d shows the HRTEM image of NRGO-$CoWO_4$-Fe_2O_3 wherein, the formation of heterojunction interface between $CoWO_4$ and Fe_2O_3 on the edges of the NRGO nanosheets is seen. The obtained lattice fringe of 0.467 nm matched with the (001) plane of $CoWO_4$ and 0.268 nm corresponded to the (104) plane of Fe_2O_3. Therefore, it is far more evident that the interface is fashioned with the Fe_2O_3 (104) plane and the $CoWO_4$ (001) planes and are stacking on the NRGO sheets. The average particle size distribution of the nanoparticles was found to be 19.02 nm for $CoWO_4$ and 7.74 nm for Fe_2O_3 (Fig. S3). Further, uniform distributions of elements, N, C, O, Co, Fe and W are shown in the elemental color mapping image, Fig. S4.

The optical characteristics of the as-synthesized nanocomposites were examined by using the UV-Visible diffuse reflectance spectroscopy (DRS). The absorbances of all the samples are in the visible region (Fig. 5a). When Fe_2O_3 nanoparticles are added to NRGO-$CoWO_4$ the range and the extent to which the composite absorbs in the visible region increases compared to the component materials. This, in turn makes the ternary composite more efficient in photocatalytic degradation of organic pollutants. The band gaps of the materials are shown in Fig. S5.

The band gap energy was estimated employing Tauc approach (equation 3) from plots of $(\alpha h\nu)^2$ versus photon energy ($h\nu$) for $CoWO_4$, NRGO-$CoWO_4$, Fe_2O_3, $CoWO_4$-Fe_2O_3 and NRGO-$CoWO_4$-Fe_2O_3 nanocomposites [8–10].

$$\alpha h\nu^{\circ} = A(h\nu - E_g)^{n/2} \quad (3)$$

where α, h, and ν are absorption coefficient, Planck's constant, the frequency of the light, respectively. n is 1 and 4 for direct and indirect band gap of semiconductors, respectively. The calculated direct band gap energies ($n = 1$) are, 2.52 eV, 2.18 eV, 2.04 eV, 1.90 eV and 1.74 eV for $CoWO_4$, NRGO-$CoWO_4$, Fe_2O_3, $CoWO_4$-Fe_2O_3 and NRGO-$CoWO_4$-Fe_2O_3 nanocomposite, respectivelyThe decrease in the band gap energy of NRGO-$CoWO_4$-Fe_2O_3 nanocomposite facilitates the material to possess excellent visible light photocatalytic activity compared to other materials.

Based on the above results, the band edge positions of the nanocomposites were calculated theoretically using the Mulliken electronegativity theory following the empirical formulae, 4 and 5 [10].

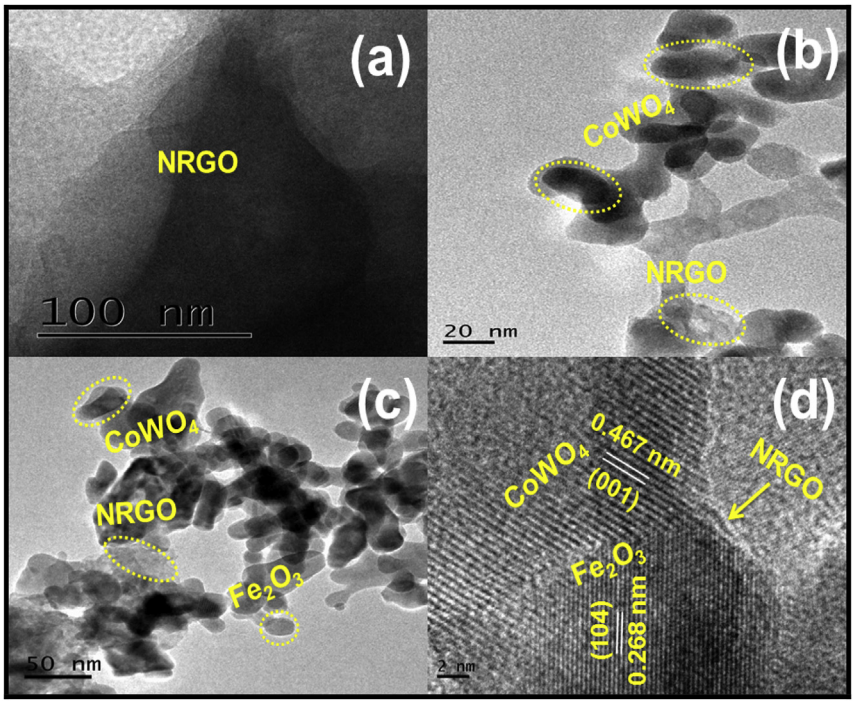

Fig. 4. TEM images of (a) NRGO, (b) NRGO-$CoWO_4$, (c) NRGO-$CoWO_4$-Fe_2O_3 and (d) HRTEM image of NRGO-$CoWO_4$-Fe_2O_3.

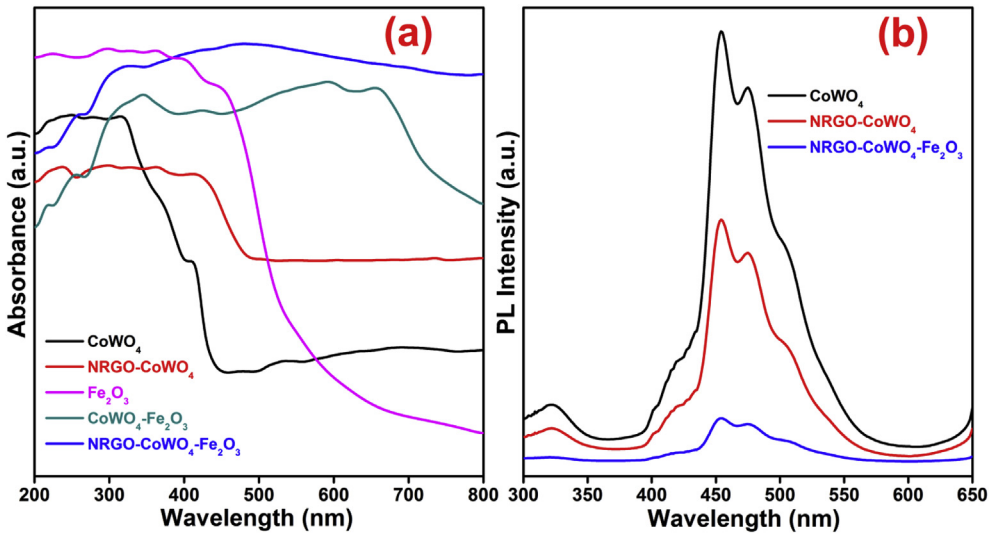

Fig. 5. (a) UV-Vis spectra of $CoWO_4$, NRGO-$CoWO_4$, $CoWO_4$-Fe_2O_3 and NRGO-$CoWO_4$-Fe_2O_3; (b) PL spectrum of $CoWO_4$, NRGO-$CoWO_4$ and NRGO-$CoWO_4$-Fe_2O_3.

$$E_{VB} = \chi - E^e + 0.5E_g \quad (4)$$

$$E_{CB} = E_{VB} - E_g \quad (5)$$

where E_{VB}, E_{CB} and E_g are the valence band (VB) edge potential, conduction band (CB) edge potential, band gap energy of the semiconductor, E^e is the scale factor of the hydrogen reference electrode (-4.5 eV) and χ is the absolute electronegativity of the semiconductor, which is defined as the geometric mean of absolute electronegativity of the constituent atoms. The calculated band edge of CB and VB potential of $CoWO_4$ and Fe_2O_3 are listed in Table S2. The band gap energy of the bare $CoWO_4$ is determined to be 2.52 eV. The calculated band edge of E_{CB} and E_{VB} are 0.517 eV and 3.037 eV, respectively. For Fe_2O_3, the band edge values of E_{CB} (0.366 eV) and E_{VB} (2.406 eV) are slightly lesser than that of $CoWO_4$. This type of energy band gap alignment corresponds to type-II junction architecture and results in efficient charge separation and hence enhanced photocatalytic activity.

The photocatalytic activities of ternary nanocomposites are assumed to be due to better separation of photogenerated electrons and holes. The charge carrier separation and recombination of photogenerated electron-holes in the ternary nanocomposite were investigated through PL emission spectrum. The PL spectra of the $CoWO_4$, NRGO-$CoWO_4$ and NRGO-$CoWO_4$-Fe_2O_3 are shown in Fig. 5b. If the recombination rate is lesser, then the PL intensity would be lesser. All the samples exhibited a broad emission peak in the visible region starting from 300 nm to 650 nm with an excitation wavelength of about 280 nm. The pure $CoWO_4$ has an intense peak around 453 nm corresponding to the recombination of photo generated electron-holes [10]. With introduction of NRGO the intensity of PL slightly decreased due to the increase in trapping states at the surface defect of NRGO-$CoWO_4$ nanocomposite. Further introduction of Fe_2O_3 made the PL intensity very weak due to the synergistic effect of both $CoWO_4$ and Fe_2O_3 with the NRGO interlayer in reducing the recombination of electron hole pairs.

3.3. Photocatalytic activity

The photocatalytic activity of NRGO-$CoWO_4$-Fe_2O_3 ternary nanocomposite was assessed by the photocatalytic dye degradation of MB using the visible light source. In order to optimize the composition of NRGO and Fe_2O_3 in the nanocomposite, initially we prepared and analyzed the activities of NRGO-$CoWO_4$ composites with NRGO amount varying from 0.5% to 5%. The nanocomposite with 2.5% NRGO showed highest activity and hence the nanocomposite with 2.5% NRGO was used for the preparation of ternary composites with varying concentrations of Fe_2O_3 precursor, ferric nitrate solution (0.005–0.02 M). The nanocomposite with composition 2.5% NRGO and Fe_2O_3 content of 0.01 M (in terms of ferric nitrate solution strength) showed maximum photocatalytic activity in the degradation of MB dye. Hence the nanocomposite with this composition was considered as the optimized sample and used for further studies. Fig. 6a shows the results in the form of C/C_o versus time plot. Blank test (control) was performed without the addition of nanocomposite and there was no noticeable degradation indicating that the photolysis of MB was negligible. The photocatalytic dye degradation efficiency of MB solutions in the presence of NRGO, $CoWO_4$, NRGO-$CoWO_4$, $CoWO_4$-Fe_2O_3 and NRGO-$CoWO_4$-Fe_2O_3 were about 17.35%, 22.68%, 59.40%, 72.26% and 99.05% under visible light irradiation in time duration of 120 min. The obtained results show that the NRGO-$CoWO_4$-Fe_2O_3 ternary nanocomposites have excellent photocatalytic degradation efficiency than that of pure NRGO, $CoWO_4$, NRGO-$CoWO_4$ and $CoWO_4$-Fe_2O_3 and that the photocatalytic degradation efficiency of the $CoWO_4$ is significantly enhanced by NRGO and Fe_2O_3.

The as-prepared ternary nanocomposites followed the first order kinetics of the photocatalytic degradation of MB dye [8,9] as given in equation (6).

$$-\ln(C/C_o) = kt \quad (6)$$

where, C is the initial concentration of the MB dye, C_o is the concentration of MB at irradiation time 't' and k is the first order rate constant. Fig. 6b gives the rate constant 'k' values calculated from the slope of the straight lines obtained when equation (6) is plotted. As can be seen from the values that the rate constant of the NRGO-$CoWO_4$-Fe_2O_3 is relatively high, in comparison to the other samples such as pure NRGO, $CoWO_4$, NRGO-$CoWO_4$ and $CoWO_4$-Fe_2O_3 composites.

In order to verify that the removal of MB is a process of photocatalytic degradation leading to complete mineralization of the dye, we have determined the total organic carbon content (TOC) of the reaction medium during the photo catalysis process [8]. Using the

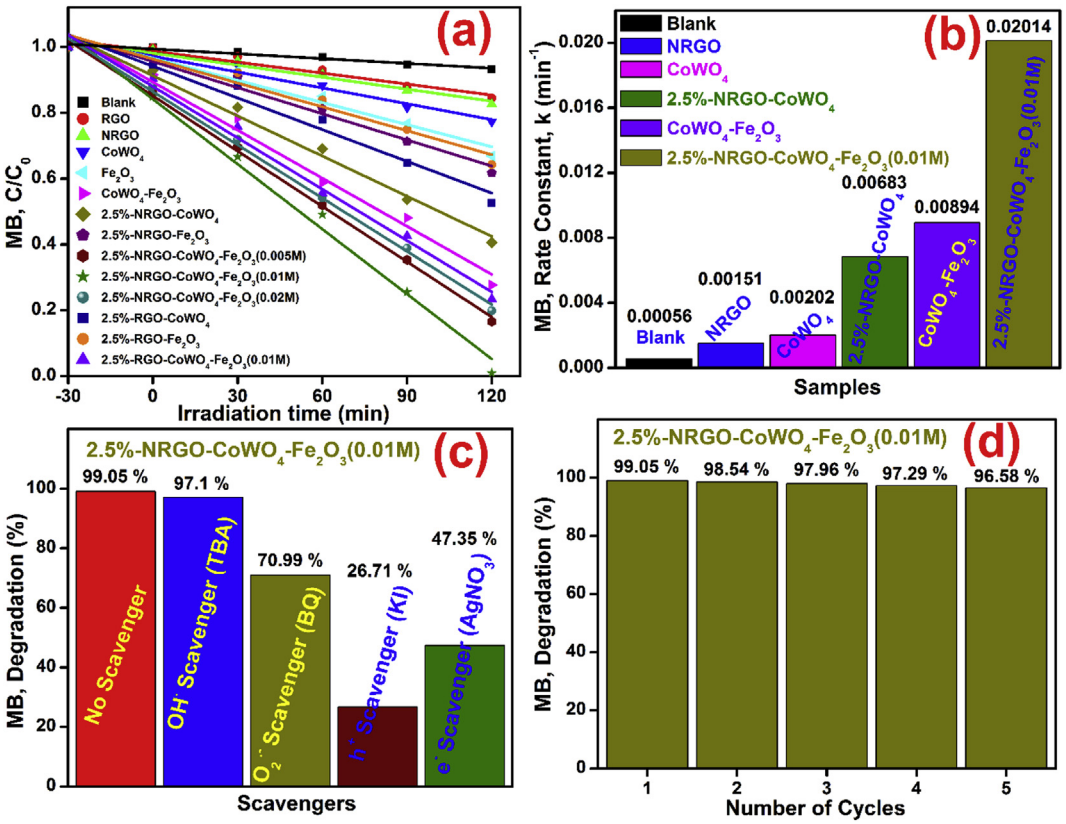

Fig. 6. (a) Degradation plots of MB over various catalysts under visible light irradiation, (b) First order rate constants for photodegradation of MB over various catalysts under visible light irradiation, (c) Plot depicting effects of different scavengers on degradation efficiency by NRGO-$CoWO_4$-Fe_2O_3 under visible light irradiation and (d) Reusability test plots.

TOC values, percentage mineralization of the dye was calculated employing equation (2) as given earlier. The mineralization test results are shown in the form of a bar diagram in Fig. 7. As can be observed from the figure, it is evident that the mineralization value increased to 86.12% in 120 min or TOC content decreased to 13.88% indicating that the organic carbon is mostly converted to CO_2 during the process. In view of this, it can be concluded that the nanocomposite is an eco-friendly photocatalyst.

Also, to confirm further, that photocatalysis leads to degradation of the dye, we carried out mass spectroscopic (MS) studies of the photocatalytic degradation intermediate products and the results are shown in Fig. 8. Mass spectra of pure MB is shown in the inset of Fig. 8. Many peaks of different intensities were observed in addition to the very weak molecular ion peak of MB dye. Some of the identified intermediates are, azure A ($m/z = 270$), azure B ($m/z = 256$), azure C ($m/z = 242$), 2-amino-5-(N-methyl formamide)-benzene sulfonic acid ($m/z = 230$), thionin ($m/z = 228$), 2-amino-5-(methyl amino)-hydroxybenzene sulfonic acid ($m/z = 218$),

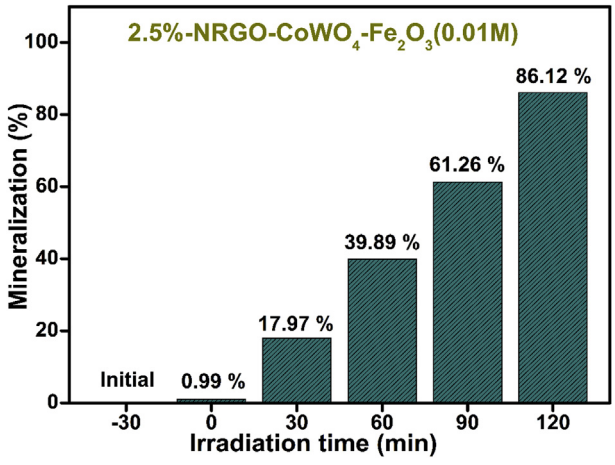

Fig. 7. Plot depicting percentage of mineralization.

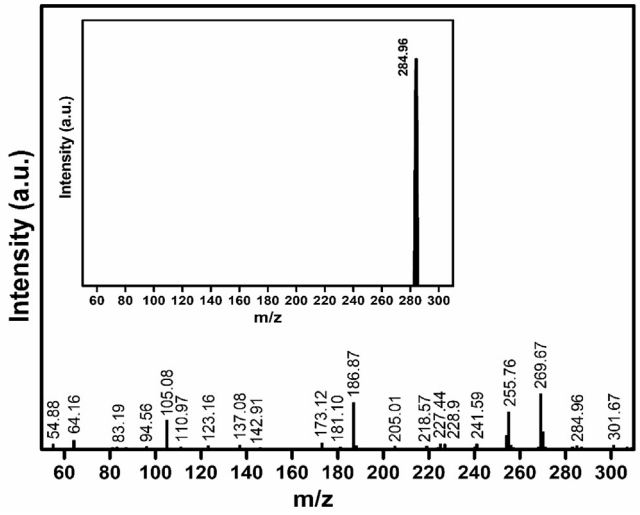

Fig. 8. Mass spectrum of MB dye after 120 min of photocatalytic degradation reaction using NRGO-$CoWO_4$-Fe_2O_3 under visible light irradiation. Inset: Mass spectra of original MB.

benzenesulfonic acid ($m/z = 158$), and phenol ($m/z = 94$). Thus, the results confirm that the catalyst efficiently degrades the dye. The results are also in agreement with the reported studies [31,32].

To find out the active species involved in photocatalytic degradation, reactions were carried out via the trapping experiments. A series of quenchers consisting of benzoquinone (1 mM, BQ) as a scavenger for O_2^-, potassium iodide (10 mM, KI) as a scavenger for h^+, silver nitrate (10 mM, $AgNO_3$) as a scavenger for e^- and ternary butanol (10 mM, TBA) as a scavenger for $OH^·$ were added to the MB solution before the addition of nanocomposite to determine the dominant active species. For the ternary nanocomposites, the addition of TBA (hydroxyl radical scavenger) causes a small decrease in photocatalytic degradation efficiency and hence it can be assumed that it is not the main active species (Fig. 6c). On the contrary the addition of KI (hole scavenger), $AgNO_3$ (electron scavenger) and the BQ (superoxide radical anion scavenger) led to extreme decrease in the efficiency in that order. Hence it can be concluded that holes are the major species in this catalyst system influencing the photo degradation.

To assess the usefulness of the catalyst, we have studied the catalytic stability and reusability of the NRGO-$CoWO_4$-Fe_2O_3 nanocomposite. The catalyst was recovered from the previous reaction mixture, washed with 10% ethanol, then dried in a vacuum oven for 6 h at 60 °C. The reused catalyst exhibited excellent catalytic activity even after 5 successive cycles (Fig. 6d), with small loss of activity which is 2.5% which is acceptable for practical applications.

For the ternary nanocomposites, the improved photocatalytic degradation performance may be well ascribed to the synergetic contribution of Fe_2O_3, $CoWO_4$ and NRGO. The photocatalytic degradation mechanism follows equations (7–10).

$$Fe_2O_3 + h\nu \rightarrow Fe_2O_3\left(e^-_{CB} + h^+_{VB}\right) \quad (7)$$

$$Fe_2O_3\ (e^-_{CB}) + CoWO_4 \rightarrow Fe_2O_3 + CoWO_4(e^-_{CB}) \quad (8)$$

$$CoWO_4\ (e^-_{CB}) + O_2 \rightarrow CoWO_4 + O_2^- \quad (9)$$

$$Fe_2O_3\left(h^+_{VB}\right) + MB \rightarrow CO_2 + H_2O \quad (10)$$

where e^-_{CB} is the electron in the conduction band and h^+_{VB} is the holes in the valence band, respectively.

The schematic diagram depicting the mechanism of photocatalytic degradation in the presence of ternary nanocomposites is shown in Fig. 9. When NRGO-$CoWO_4$-Fe_2O_3 is irradiated with visible light, first the electrons are excited from the valence band (VB) to the conduction band (CB) of the Fe_2O_3. Then, the electrons from the conduction band of Fe_2O_3 move to the conduction band of $CoWO_4$ and then get transported through NRGO interlayer for reduction of oxygen. The holes will immediately react with MB to yield harmless products like CO_2 and H_2O. Thus, the recombination of photo generated electron-hole pairs is prevented and results in improved photocatalytic degradation performance of the synthesized ternary nanocomposites. The results also suggest that these ternary nanocomposites materials could be promising candidates for various environmental applications.

3.4. Hydrogenation activity

The catalytic activity of NRGO-$CoWO_4$-Fe_2O_3 nanocomposite with optimized composition of NRGO and Fe_2O_3 towards hydrogenation was evaluated by the reduction of 4-NP using $NaBH_4$ in an aqueous solution. Blank test was performed in the absence of the nanocomposite which revealed negligible reduction. However, when NRGO-$CoWO_4$-Fe_2O_3 nanocomposite was added to the 4-NP solution, the absorption of 4-NP found at 400 nm peak decreased immediately and the new absorption peak of 4-AP appeared at 300 nm which increased in intensity with time as shown in Fig. 10a. The catalytic reduction of 4-NP to 4-AP took 30 s to undergo completion which could also be seen visually in the form of color change from bright yellow to colorless (inset Fig. 10a) [24]. The efficiency of the ternary composite is compared with the component materials NRGO, $CoWO_4$, NRGO-$CoWO_4$ and $CoWO_4$-Fe_2O_3. The component materials show lower activity than the ternary composite as shown in Fig. 10b indicating that introduction of NRGO improves the reduction efficiency of $CoWO_4$-Fe_2O_3.

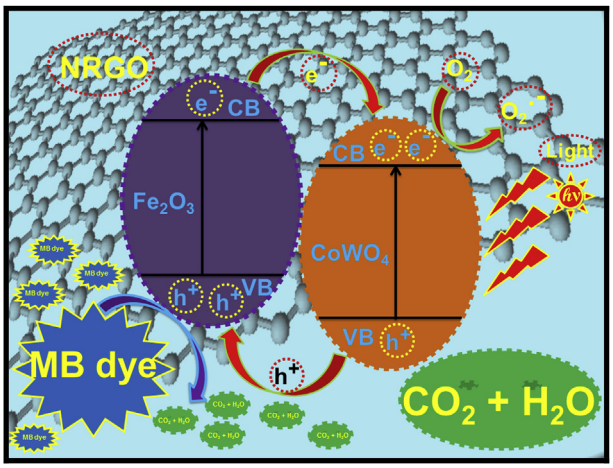

Fig. 9. Schematic diagram showing mechanism for photodegradation of MB using NRGO-$CoWO_4$-Fe_2O_3 under visible light irradiation.

The reaction followed first order kinetics with respect to 4-NP concentration [24]. The reaction kinetics can be expressed by the relation, $-\ln(C/C_o) = kt$, where k and t are the rate constant at a given temperature and reaction time, respectively. C_o, C are the 4-NP concentration at the beginning and at time t, respectively. The first order rate constants (k) obtained from the slopes of $-\ln(C/C_o)$ vs. time plots for all the materials are shown in Fig. 10c.

It is obvious that, among all the catalysts, NRGO-$CoWO_4$-Fe_2O_3 nanocomposite exhibits the maximum rate constant of 0.08438 s^{-1}, which is 2.3 times that of $CoWO_4$-Fe_2O_3 (0.03620 s^{-1}), 3.5 times that of NRGO-$CoWO_4$ (0.02435 s^{-1}), 4.5 times that of $CoWO_4$ (0.01883 s^{-1}), which demonstrates the extremely good catalytic activity of NRGO-$CoWO_4$-Fe_2O_3 nanocomposite. The above results clearly indicate that NRGO-$CoWO_4$-Fe_2O_3 nanocomposite exhibits a significantly enhanced catalytic activity compared to that of unsupported $CoWO_4$-Fe_2O_3 as a result of the introduction of NRGO.

The catalytic stability and reusability of the NRGO-$CoWO_4$-Fe_2O_3 nanocomposite were carried out by extracting the catalyst from the previous reaction, washing it with 10% ethanol, later drying it in a vacuum oven for 6 h at 60 °C. The reused catalyst exhibited excellent catalytic activity even after 10 successive cycles, with nearly 100% conversion within a time period of 60 s (Fig. 10d).

4. Conclusions

In this work, we report the preparation of NRGO-$CoWO_4$-Fe_2O_3 ternary nanocomposite by microwave irradiation method and its characterization by XRD, TEM, HRTEM, XPS, BET, Raman, PL and UV-Visible spectroscopy. The composite was studied for its photocatalytic activity on MB dye under visible light irradiation and for reduction of 4-NP to 4-AP using $NaBH_4$. The catalytic efficiency and

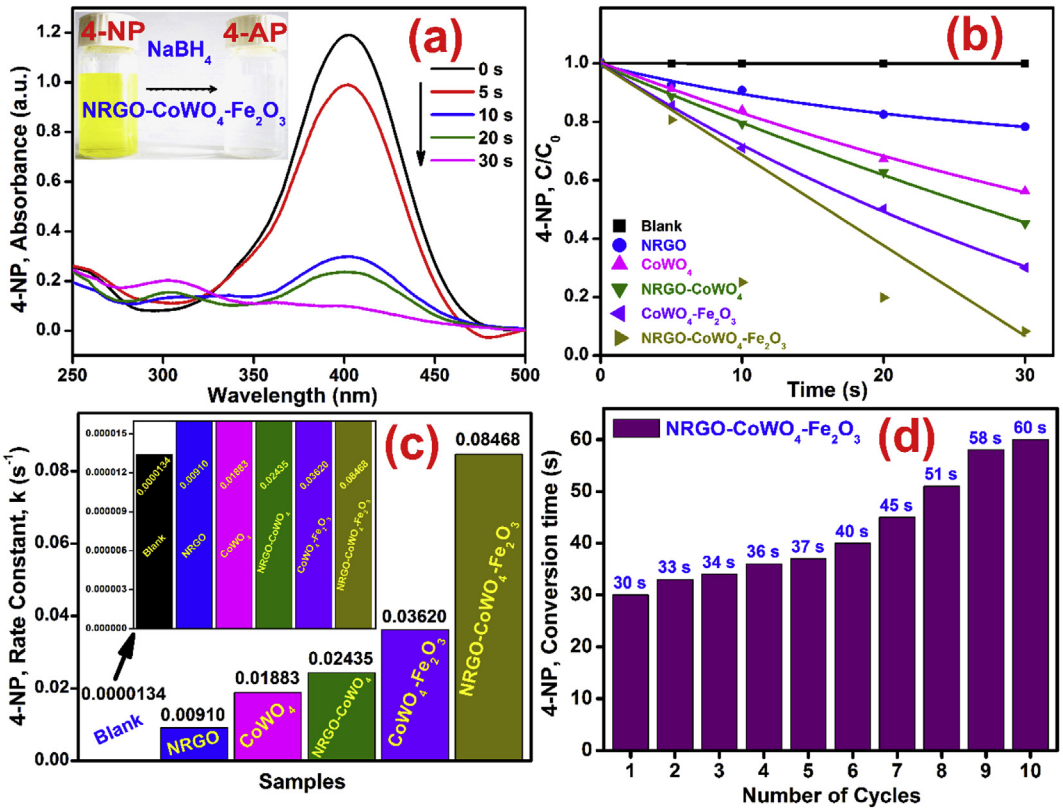

Fig. 10. (a) Absorption plot showing reduction of 4-NP to 4-AP using NRGO-$CoWO_4$-Fe_2O_3 nanocomposites, (b) Relative concentration plots for reduction of 4-NP to 4-AP using different catalysts, (c) First order rate constants for reduction of 4-NP to 4-AP using different catalysts and (d) Reusability test plots.

rate constant of NRGO-$CoWO_4$-Fe_2O_3 show better activity in comparison to other composites generally used for the purpose. Based on the experimental results, possible mechanism for photodegradation is also proposed. The study indicates that this novel nanocomposite could be a potential candidate for various environmental applications.

Acknowledgments

M.J.S.M. is grateful to the National Institute of Technology Karnataka, Surathkal, Mangalore, for financial support in the form of Institute Fellowship.

Appendix A. Supplementary data

Supplementary data related to this article can be found at https://doi.org/10.1016/j.matchemphys.2018.01.012.

References

[1] T. Hisatomi, J. Kubota, K. Domen, Recent advances in semiconductors for photocatalytic and photoelectrochemical water splitting, Chem. Soc. Rev. 43 (2014) 7520–7535.
[2] L. Zhang, H.H. Mohamed, R. Dillert, D. Bahnemann, Kinetics and mechanisms of charge transfer processes in photocatalytic systems: a review, J. Photochem. Photobiol. C Photochem. Rev. 13 (2012) 263–276.
[3] A.D. Paola, E.G. Lopez, G. Marci, L.A. Palmisano, Survey of photocatalytic materials for environmental remediation, J. Hazard Mater. 211-212 (2012) 3–29.
[4] A. Mills, S. Le Hunte, An overview of semiconductor photocatalysis, J. Photochem. Photobiol. Chem. 108 (1997) 1–35.
[5] A.S. Bhatt, D.K. Bhat, C. Tai, M.S. Santosh, Microwave-assisted synthesis and magnetic studies of cobalt oxide nanoparticles, Mater. Chem. Phys. 125 (2011) 347–350.
[6] S.K. Dutta, S.K. Mehetor, N. Pradhan, Metal semiconductor heterostructures for photocatalytic conversion of light energy, J. Phys. Chem. Lett. 6 (2015) 936–944.
[7] S.T. Kochuveedu, Y.H. Jang, D.H. Kim, A study on the mechanism for the interaction of light with noble metal-metal oxide semiconductor nanostructures for various photophysical applications, Chem. Soc. Rev. 42 (2013) 8467–8493.
[8] M.M.J. Sadiq, S.U. Shenoy, D.K. Bhat, $NiWO_4$-ZnO-NRGO ternary nanocomposite as an efficient photocatalyst for degradation of methylene blue and reduction of 4-nitro phenol, J. Phys. Chem. Solid. 9 (2017) 124–133.
[9] M.M.J. Sadiq, S.U. Shenoy, D.K. Bhat, Enhanced photocatalytic performance of N-doped RGO-$FeWO_4$/Fe_3O_4 ternary nanocomposite in environmental applications, Mater. Today Chem. 4 (2017) 133–141.
[10] M.M.J. Sadiq, S.U. Shenoy, D.K. Bhat, Novel RGO-$ZnWO_4$-Fe_3O_4 nanocomposite as high performance visible light photocatalyst, RSC Adv. 6 (2016) 61821–61829.
[11] L. Wang, J. Ding, Y. Chai, Q. Liu, J. Ren, X. Liu, W.L. Dai, CeO_2 nanorod/g-C_3N_4/N-rGO composite: enhanced visible-light-driven photocatalytic performance and the role of N-rGO as electronic transfer media, Dalton Trans. 44 (2015) 11223–11234.
[12] N. Zhang, Y. Zhang, Y.J. Xu, Recent progress on graphene-based photocatalysts: current status and future perspectives, Nanoscale 4 (2012) 5792–5813.
[13] A. Alborzi, A. Abedini, Synthesis, characterization and investigation of magnetic and photocatalytic property of cobalt tungstate nanoparticles, J. Mater. Sci. Mater. Electron. 27 (2016) 4057–4061.
[14] D.R. Kumar, S. Karuppuchamy, Microwave mediated synthesis of nanostructures $CoWO_3$ and $CoWO_4$ for supercapacitor applications, J. Alloy. Comp. 674 (2016) 384–391.
[15] X. Xu, J. Shen, N. Li, M. Ye, Facile synthesis of reduced graphene oxide/$CoWO_4$ nanocomposites with enhanced electrochemical performances for supercapacitors, Electrochim. Acta 150 (2014) 23–34.
[16] B. Subramanya, D.K. Bhat, Novel eco-friendly synthesis of graphene directly from graphite using TEMPO and study of its electrochemical properties, J. Power Sources 275 (2015) 90–98.
[17] S.Z. Butler, S.M. Hollen, L. Cao, Y. Cui, J.A. Gupta, H.R. Gutierrez, T.F. Heinz, S.S. Hong, J. Huang, A.F. Ismach, Progress, challenges, and opportunities in two-dimensional materials beyond graphene, Action Natl. 7 (2013) 2898–2926.
[18] Y. Zhu, S. Murali, W. Cai, X. Li, J.W. Suk, J.R. Potts, R.S. Ruoff, Graphene and graphene oxide: synthesis, properties, and applications, Adv. Mater. 22 (2010) 3906–3924.
[19] X. Huang, X. Qi, F. Boey, H. Zhang, Graphene-based composites, Chem. Soc.

Rev. 41 (2012) 666–686.
[20] H. Chang, H. Wu, Graphene-based nanocomposites: preparation, functionalization and energy and environmental applications, Energy Environ. Sci. 6 (2013) 3483–3507.
[21] B. Subramanya, D.K. Bhat, S.U. Shenoy, Y. Ullal, A.C. Hegde, Novel Fe-Ni-Graphene composite electrode for hydrogen production, Int. J. Hydrogen Energy 40 (2015) 10453–10462.
[22] B. Subramanya, Y. Ullal, S.U. Shenoy, D.K. Bhat, A.C. Hegde, Novel Co-Ni-graphene composite electrodes for hydrogen production, RSC Adv. 5 (2015) 47398–47407.
[23] X. Li, H. Wang, J.T. Robinson, H. Sanchez, G. Diankov, H. Dai, Simultaneous nitrogen doping and reduction of graphene oxide, J. Am. Chem. Soc. 131 (2009) 15939–15944.
[24] M.M.J. Sadiq, D.K. Bhat, Novel RGO-$ZnWO_4$-Fe_3O_4 nanocomposite as an efficient catalyst for rapid reduction of 4-nitrophenol to 4-aminophenol, Ind. Eng. Chem. Res. 55 (2016) 7267–7272.
[25] M. Khandelwal, A. Kumar, One-step chemically controlled wet synthesis of graphene nanoribbons from graphene oxide for high performance supercapacitor applications, J. Mater. Chem. 3 (2015) 22975–22988.
[26] C. Fu, C. Song, L. Liu, X. Xie, W. Zhao, Synthesis and properties of nitrogen-doped graphene as anode materials for lithium-ion batteries, Int. J. Electrochem. Sci. 11 (2016) 3876–3886.
[27] T. Szabo, O. Berkesi, P. Forgo, K. Josepovits, Y. Sanakis, D. Petridis, I. Dékány, Evolution of surface functional groups in a series of progressively oxidized graphite oxides, Chem. Mater. 18 (2006) 2740–2749.
[28] A.C. Ferrari, D.M. Basko, Raman spectroscopy as a versatile tool for studying the properties of graphene, Nat. Nanotechnol. 8 (2013) 235–246.
[29] Q. Wei, Z. Zhang, Z. Li, Q. Zhou, Y. Zhu, Enhanced photocatalytic activity of porous α-Fe_2O_3 films prepared by rapid thermal oxidation, J. Phys. Appl. Phys. 41 (2008), 202002(1-4).
[30] Y. Liu, F. Pei, R. Lu, S. Xu, S. Cao, TiO_2/N-graphene nanocomposite via a facile in-situ hydrothermal sol-gel strategy for visible light photodegradation of eosin Y, Mater. Res. Bull. 60 (2014) 188–194.
[31] C. Yang, W. Dong, G. Cui, Y. Zhao, X. Shi, X. Xia, B. Tang, W. Wang, Highly efficient photocatalytic degradation of methylene blue by P2ABSA-modified TiO_2 nanocomposite due to the photosensitization synergetic effect of TiO2 and P2ABSA, RSC Adv. 7 (2017) 23699–23708.
[32] S. Xia, L. Zhang, G. Pan, P. Qian, Z. Ni, Photocatalytic degradation of methylene blue with nanocomposite system: synthesis, photocatalysis and degradation pathways, Phys. Chem. Chem. Phys. 17 (2015) 5345–5351.